

Analyzing Tomographic SAR Data of a Forest With Respect to Frequency, Polarization, and Focusing Technique

Othmar Frey, *Member, IEEE*, and Erich Meier, *Associate Member, IEEE*

Abstract—Forest canopies are semitransparent to microwaves at both L- and P-bands. Thus, a number of scattering sources and different types of scattering mechanisms may contribute to a single range cell of a synthetic aperture radar (SAR) image. By appropriately combining the SAR data of multiple parallel flight paths, a large 2-D aperture is synthesized, which allows for tomographic imaging of the 3-D structure of such semitransparent media and the underlying ground. A separate paper deals with the actual tomographic imaging part that leads to the 3-D data cube. In particular, three focusing techniques are described and analyzed: multilook beamforming, robust Capon beamforming, and multiple signal classification beamforming. In this paper, the resulting data products obtained by tomographically focusing two airborne multibaseline SAR data sets of a partially forested area, one at L-band and another at P-band, are subject to a detailed analysis with respect to the location and the type of backscattering sources. In particular, the following aspects are investigated: 1) The forest structure, as obtained from the vertical profiles of intensities at sample plot locations within the forest, is compared to the height distribution of the top of the forest canopy, as derived from airborne laser scanning data, and profiles are presented for all polarimetric channels and focusing techniques, as well as at both frequencies; 2) the type and location of scattering mechanisms are analyzed as functions of height for the two frequencies, namely, L- and P-bands, and using the polarimetric channels, as well as the Pauli and Cloude–Pottier decompositions thereof; and 3) the accuracy of the ground elevation estimation obtained from the different focusing techniques and the two frequencies is assessed with the help of a lidar-derived digital elevation model.

Index Terms—Airborne radar, backscattering mechanisms, beamforming, Capon beamformer, forestry, L-band, multibaseline, multiple signal classification, P-band, polarimetry, SAR tomography, synthetic aperture radar (SAR), time-domain back-projection (TDBP).

Manuscript received June 17, 2010; revised December 6, 2010; accepted January 22, 2011. Date of publication April 18, 2011; date of current version September 28, 2011. This work was supported by the Procurement and Technology Center (armasuisse) of the Swiss Federal Department of Defense.

O. Frey was with the Remote Sensing Laboratories, University of Zurich, 8057 Zurich, Switzerland. He is now with the Chair of Earth Observation and Remote Sensing, Institute of Environmental Engineering, Swiss Federal Institute of Technology (ETH) Zurich, 8093 Zurich, Switzerland, and also with GAMMA Remote Sensing AG, 3073 Gümligen, Switzerland (e-mail: ofrey@ethz.ch).

E. Meier is with the Remote Sensing Laboratories, University of Zurich, 8057 Zurich, Switzerland (e-mail: erich.meier@geo.uzh.ch).

Color versions of one or more of the figures in this paper are available online at <http://ieeexplore.ieee.org>.

Digital Object Identifier 10.1109/TGRS.2011.2125972

I. INTRODUCTION

RESEARCH toward improving the knowledge about the backscattering behavior of forests by means of synthetic aperture radar (SAR) tomography with the eventual goal of estimating its biophysical parameters has become a major topic within the SAR remote sensing community [1]–[15].

With three prospective spaceborne SAR remote sensing missions, namely, BIOMASS [16], [17] at P-band and Tandem-L [18], [19] and DESDynI [20] at L-band, which are all aimed at global mapping and monitoring of carbon stock by assessing the above-ground biomass of forests, as well as forest dynamics such as the amount of deforestation and regrowth, these two frequency bands have gained importance. Establishing a good understanding of the interaction of microwaves at L- and P-bands with vegetation, and in particular, with forests, is a prerequisite in order to develop reliable biomass products.

As has been stated in [1] and [21]–[23], a simple backscattering-based measurement of biomass is not feasible for dense forested areas due to saturation levels around 100 t/ha at L-band and 200 t/ha at P-band. Inevitably, additional measures, such as forest height (involving the extraction of the underlying terrain height) and structural information about the forest, are to be incorporated into an improved estimation of forest biomass.

Although a number of publications treat advanced algorithms for tomographic SAR imaging (see, e.g., [24]–[37]), much less research has been done that actually incorporates and evaluates real tomographic SAR data of forested areas. In particular, this is the case for P-band data. In [6], backscattering profiles of a forest extracted from tomographic L-band SAR data were shown, and the additional benefit of 3-D imaging of forests was highlighted. Excerpts of the same L-band data set are also used in [38], where the superior performance of the Capon beamformer with respect to spectral-analysis-based beamforming is demonstrated. In [39], fast Fourier transform, Capon, and multiple signal classification (MUSIC) beamforming approaches based on the deramping and spectral estimation scheme of a stack of coregistered single-look complex images are discussed.

In September 2006, an airborne SAR campaign was flown by the German Aerospace Center's E-SAR system over a test site in Switzerland. Two fully polarimetric tomographic data sets (L- and P-bands) of a partially forested area were taken within this campaign (see Table I for the sensor specifications and a summary of the parameters which characterize the tomographic data sets). Using these data, the first tomographic images of

TABLE I
E-SAR SYSTEM SPECIFICATIONS AND NOMINAL PARAMETERS OF
THE TOMOGRAPHIC ACQUISITION PATTERNS FOR
BOTH MB DATA SETS AT P- AND L-BANDS

	P-band	L-band
Carrier frequency	350 MHz	1.3 GHz
Chirp bandwidth	70 MHz	94 MHz
Sampling rate	100 MHz	100 MHz
PRF	500 Hz	400 Hz
Ground speed	90 m/s	90 m/s
No. of data tracks	11+1	16+1
Nominal track spacing d_n	57 m	14 m
Horizontal baselines	40 m	10 m
Vertical baselines	40 m	10 m
Synthetic aperture in normal direction L	570 m	210 m
Nominal resolution in normal direction δ_n	3 m	2 m
Approx. unambiguous height H	30 m	30 m

a forest at P-band were presented by Frey *et al.* [10], [11]. The HH polarization channel of the multibaseline (MB) P-band data set was tomographically focused using a time-domain back-projection (TDBP) approach, and a qualitative comparison with an airborne laser scanning (ALS) digital elevation model (DEM)/digital surface model (DSM) data set was carried out. In [40], the TDBP-based focusing methodology was extended toward multilook-based standard and Capon beamforming.

In [12], data from another MB data set at L-band, also acquired in 2006, were used to experimentally test a method, based on the prolate spheroidal wave functions, to estimate the dimension of the signal subspace for MUSIC beamforming in order to determine the minimum number of baselines needed for tomographic focusing of a forest scenario.

Most recently, Tebaldini [15] has proposed a theoretical framework to separate different scattering mechanisms based on polarimetric MB SAR data. Experimental results were provided using an airborne P-band data set acquired during the BioSAR campaign in 2007. In contrast to the tomographic SAR data evaluated in this paper, Tebaldini employed a rather high number of looks (350 looks) to focus the data in the normal direction, leading to a drastic loss of resolution in the range/azimuth domain. In particular, detailed features such as gaps in the canopy due to forest roads or smaller glades and clear cuts are lost to a large extent.

As documented in the recommendations of the PolInSAR 2009 workshop [41], there is still a need for research about the interactions of microwaves at different frequencies with forested areas. The vertical forest structure and terrain reflectivity under vegetated canopies need to be investigated, including the polarimetric signature.

A. Aim of This Paper

This paper attempts to contribute some pieces to diminish this research gap by providing a detailed analysis of the localization of the main backscattering elements within a 3-D SAR data cube. The focused data were obtained by means of nonmodel-based¹ tomographic processing of two airborne fully

¹Nonmodel based in the sense that no forest model is used. However, MUSIC is a model-based direction-of-arrival estimator in the sense that the number of scattering sources is assumed to be known.

polarimetric MB SAR data sets of the same forested area at both L- and P-band frequencies (see Table I for the specifications). Based on a TDBP approach [42] to a reconstruction grid, three different tomographic focusing techniques, namely, multilook standard beamforming, robust Capon beamforming (RCB), and MUSIC, were applied to the data. For a detailed description of the data processing, an analysis of the focusing performance, and tomographic images of the forest, see the companion paper [43].

In this paper, the emphasis is laid on investigating the vertical structure of the forest and its underlying terrain as it appears in the two remotely sensed MB SAR data sets. To this end, the focused 3-D SAR data cubes are analyzed with respect to the following: 1) the location of the main scattering sources within the forested area at the two frequencies with the help of vertical profiles; 2) the type of scattering mechanisms [using the Cloude–Pottier decomposition (CPD)] as a function of height above ground; and 3) the accuracy of the detection of the ground below forest at L- and P-bands using the three different focusing techniques. The 3-D SAR data sets are evaluated and cross-validated with high-resolution DSM/DEM models derived from ALS.

To the authors' knowledge, this is the first time that a detailed analysis of tomographic SAR data sets, at both L- and P-bands, of a forested area is given in combination with high-resolution ALS cross-reference data. The authors intend to foster the discussion of the potential of L-band and/or P-band (MB) SAR for the determination of biophysical parameters of forests in the context of biomass/carbon stock assessment.

The remainder of this paper is organized as follows. In Section II, the experimental data are described, and the methods used to evaluate the tomographic data are detailed. In Section III, the backscattering profiles, as analyzed in terms of the parameters frequency, polarization channels, and scattering mechanisms, as well as in terms of the focusing technique, are presented. In Section IV, the results are discussed, and conclusions are drawn in Section V.

II. DATA AND METHODS

A. Focused Tomographic Data

In Fig. 1, the geometric configurations of the actual flight tracks for both tomographic data sets are shown. The flight direction is from east to west, and the sensor is left looking. In addition to the actual flight tracks, their projections to the horizontal plane and to the northing-height plane are also depicted. Both missions were completed by a control track.

The analyses presented in this paper start at the product level of the 3-D focused SAR data sets. The data cubes occupy an area of 400 m \times 900 m in easting and northing, respectively. For both MB data sets, three data products were generated using a TDBP-based approach in combination with the following:

- 1) coherent multilook beamforming (MLBF);
- 2) RCB;
- 3) MUSIC.

A detailed description of the time-domain-based focusing methods is given in [40] for MLBF and in a companion paper [43] for RCB and MUSIC, respectively. In each case, the

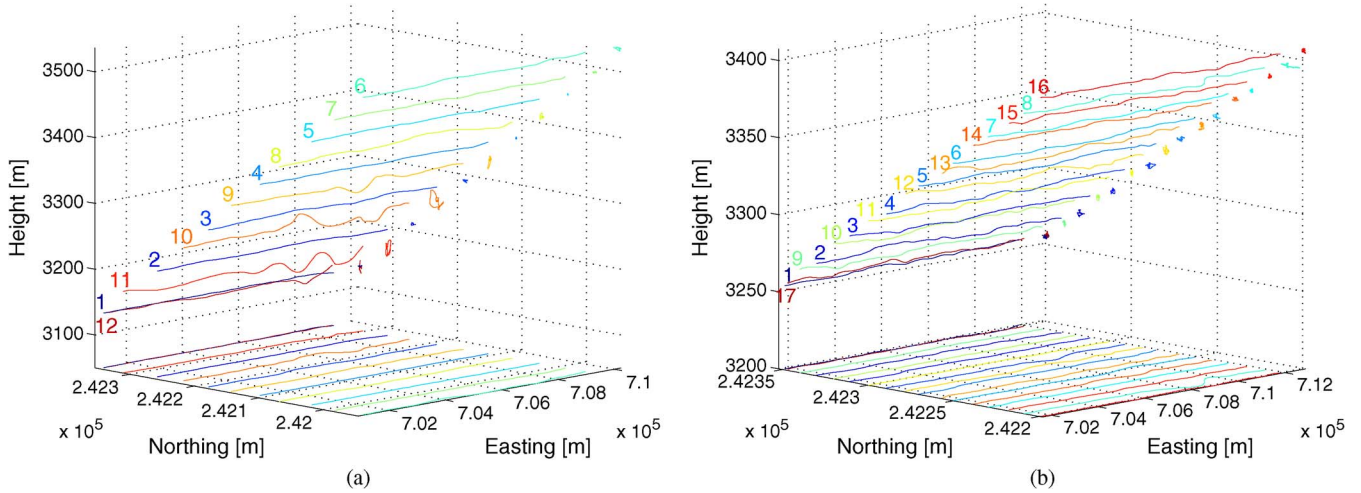


Fig. 1. Tomographic acquisition patterns (a) at P-band, consisting of 11 flight tracks and a control track, and (b) at L-band, consisting of 16 flight tracks and a control track. The flight directions are from east to west, and the sensors are left looking. In addition to the actual flight tracks, their projections to the horizontal plane and to the northing-height plane are depicted. See also Table I for additional information about the tomographic acquisition pattern.

sample covariance matrix was estimated using approximately 20 looks obtained by spatial averaging.

In our experiment, unambiguous tomographic imaging is limited to about 30 m in the direction perpendicular to the average line of sight. This constraint is a result of a tradeoff which had to be made during the design of the experimental setup of the MB data acquisition for tomographic imaging. The tradeoff is between maximizing the height resolution (a synthetic aperture in normal direction as large as possible) and maximizing the unambiguous volume height (the baselines between passes as small as possible) given a limited number of parallel flight paths due to pecuniary constraints, maximal mission time, etc. For the given test site and experimental setup, this leads to *vertical* unambiguous height values of approximately 16 to 22 m, depending on the topography and the ground range distance. The tree heights found in the forest under study go up to 40 m. The validation of the SAR tomography data is limited to sample plots where the tree height does not exceed the unambiguous height since backscattering sources that are located beyond that threshold lead to aliasing in the form of ghost targets, which spuriously appear within the unambiguous height.

B. Validation Data

External reference data in the form of a DEM derived from ALS (Falcon II, Toposys GmbH) are available for a comparison of the ground level. A DSM acquired by the same sensor is also at hand (see [43]). Both data sets are given at a sample spacing of $1 \text{ m} \times 1 \text{ m}$.

The ALS data were acquired in spring of 2003. It has to be assumed that the deciduous trees were mostly transparent to the laser signal and therefore do not appear in the lidar-derived DSM. However, the forest within the test site is dominated by evergreen coniferous trees (80% of the trees within the sample plots in the area of study are evergreen coniferous trees, predominantly Norway spruce “*Picea abies*” and European silver fir “*Abies alba*,” which make up 59% and 20% of all trees, respectively).

As the forest is managed, timber cutting took place between 2003 and 2006. Therefore, additional clear cuts had to be masked manually into the ALS DSM, based on airborne orthoimages acquired in the summer of 2006. However, cuts of single trees within forest stands are not accounted for. In order to manually insert missing deciduous trees into the DSM, another ALS-derived DSM from summer 2002 was also used.

C. Methods Used for Data Analysis

In order to analyze the backscattering behavior as a function of height above ground, the additional information contained in the polarization channels was exploited. In particular, the Pauli decomposition and the CPD (entropy/anisotropy/ α) of the polarimetric data were calculated and evaluated as a function of height above ground. In the following, the Pauli decomposition and the CPD are exposed in some detail for the sake of completeness.

1) *Pauli Decomposition*: Using the 2×2 identity matrix and the three Pauli matrices, the scattering matrix \mathbf{S} can be represented as a superposition of four coherent elementary scattering mechanisms

$$\mathbf{S} = \begin{bmatrix} S_{HH} & S_{HV} \\ S_{VH} & S_{VV} \end{bmatrix} = \frac{a}{\sqrt{2}} \mathbf{S}_a + \frac{b}{\sqrt{2}} \mathbf{S}_b + \frac{c}{\sqrt{2}} \mathbf{S}_c + \frac{d}{\sqrt{2}} \mathbf{S}_d \quad (1)$$

where

$$\begin{aligned} a &= \frac{S_{HH} + S_{VV}}{\sqrt{2}} & b &= \frac{S_{HH} - S_{VV}}{\sqrt{2}} \\ c &= \frac{S_{HV} + S_{VH}}{\sqrt{2}} & d &= i \frac{S_{HV} - S_{VH}}{\sqrt{2}} \\ \mathbf{S}_a &= \frac{1}{\sqrt{2}} \begin{bmatrix} 1 & 0 \\ 0 & 1 \end{bmatrix} & \mathbf{S}_b &= \frac{1}{\sqrt{2}} \begin{bmatrix} 1 & 0 \\ 0 & -1 \end{bmatrix} \\ \mathbf{S}_c &= \frac{1}{\sqrt{2}} \begin{bmatrix} 0 & 1 \\ 1 & 0 \end{bmatrix} & \mathbf{S}_d &= \frac{1}{\sqrt{2}} \begin{bmatrix} 0 & -i \\ i & 0 \end{bmatrix}. \end{aligned} \quad (2)$$

In the monostatic case, reciprocity applies, i.e., $S_{HV} = S_{VH}$, and thus, $d = 0$. The remaining three components a , b , and c

can be written as the elements of a 3-D target vector \mathbf{k} in the Pauli basis [44]

$$\mathbf{k} = \begin{bmatrix} a \\ b \\ c \end{bmatrix} = \frac{1}{\sqrt{2}} \begin{bmatrix} S_{HH} + S_{VV} \\ S_{HH} - S_{VV} \\ 2S_{HV} \end{bmatrix}. \quad (3)$$

The components a , b , and c stand for odd-bounce scattering (surface, trihedral reflector) and even-bounce scattering from corners with a relative orientation of 0° (dihedral) and that of 45° (tilted dihedral), respectively.

2) *CPD*: The CPD [44], [45] is based on the eigenvalue decomposition of the $\mathbf{T3}$ coherency matrix which is constructed from the outer product of the Pauli target vector \mathbf{k} and its Hermitian transpose \mathbf{k}^H

$$\mathbf{T3} = \mathbf{k}\mathbf{k}^H. \quad (4)$$

In practice, this single-look representation of the coherency matrix is rank deficient. Assuming ergodicity, a spatial average over n adjacent pixels is taken (instead of a number of snapshots), which yields the multilook coherency matrix

$$\langle \mathbf{T3} \rangle = \sum_{j=1}^n \mathbf{k}_j \mathbf{k}_j^H. \quad (5)$$

Performing the eigenvalue decomposition of the multilook coherency matrix $\langle \mathbf{T3} \rangle$ yields the eigenvalues λ_j , $j = 1 \dots 3$, sorted in nonincreasing order. Then, the first parameter of the CPD, i.e., the entropy H , is calculated as

$$H = \sum_{j=1}^3 -p_j \log_3(p_j), \quad \text{where } p_j = \frac{\lambda_j}{\sum_{m=1}^3 \lambda_m}. \quad (6)$$

$H \in [0, 1]$ is a measure for the randomness of a scattering medium from quasi-deterministic scattering ($H = 0$) to completely random scattering ($H = 1$). The second parameter, i.e., the average alpha angle α , is defined as

$$\alpha = p_1 \alpha_1 + p_2 \alpha_2 + p_3 \alpha_3 \quad (7)$$

where $\alpha_j = a \cos(u_{1j})$, as a consequence of the following parameterization of the eigenvectors \mathbf{u}_j of the coherency matrix as introduced in [45]

$$\mathbf{u}_j = [\cos \alpha_j \quad \sin \alpha_j \cos \beta_j e^{i\delta_j} \quad \sin \alpha_j \sin \beta_j e^{i\gamma_j}]^T. \quad (8)$$

The average alpha angle α indicates the averaged target scattering mechanism from surface scattering ($\alpha = 0^\circ$) over dipole scattering ($\alpha = 45^\circ$) to dihedral scattering ($\alpha = 90^\circ$), β is the target orientation angle ($-180^\circ \leq \beta < 180^\circ$), and δ and γ are the target phase angles [46]. The third parameter of the CPD, which is not used in this paper, is called anisotropy A and is calculated as $A = (p_2 - p_3)/(p_2 + p_3)$. In Fig. 2, the H/α plane is shown divided into zones representing different physical scattering characteristics according to the definitions in [45], [47]:

Z1 high-entropy multiple scattering: scattering from vegetation having a well-developed branch and crown structure;

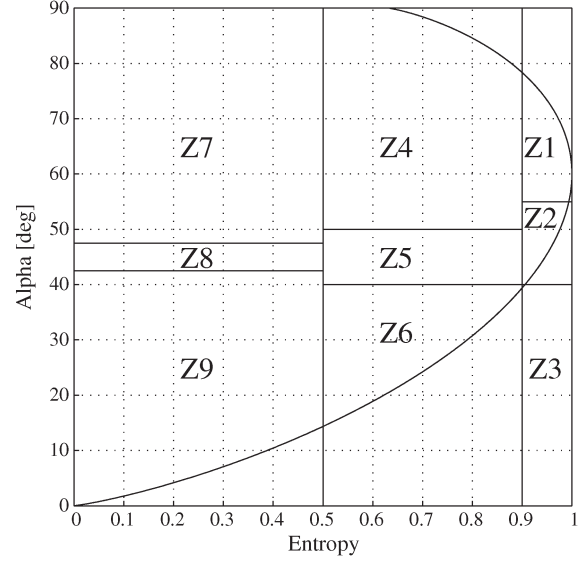


Fig. 2. Entropy/alpha classification scheme after Cloude and Pottier [45]. See Section II-C2 for a description of zones Z1–Z9. Zone 3, which is the area outside the delineating curve, represents the mathematically nonfeasible region.

- Z2 high-entropy vegetation scattering: scattering from forest canopies and scattering from vegetated surfaces with random highly anisotropic scattering elements;
- Z3 nonfeasible region;
- Z4 medium-entropy multiple scattering: dihedral scattering with moderate entropy, e.g., double bounce plus propagation through the canopy of a forest at P- and L-bands;
- Z5 medium-entropy vegetation scattering: scattering from vegetated surfaces with anisotropic scatterers and moderately correlated scatterer orientations;
- Z6 medium-entropy surface scattering: increased entropy due to surface roughness and canopy propagation;
- Z7 low-entropy multiple scattering: low-entropy double- or even-bounce scattering;
- Z8 low-entropy dipole scattering: isolated dipole scatterer or scattering from vegetation with heavily correlated orientation of anisotropic scattering elements;
- Z9 low-entropy surface scattering, e.g., water at L- and P-bands, sea-ice at L-band, and smooth land surfaces.

In the following, the CPD is used to analyze the backscattering behavior as a function of the height above ground. The scatter plots at different height levels above ground are distinguishable by different color coding. In addition, the sum of the eigenvalues of the multilook coherency matrix $\langle \mathbf{T3} \rangle$ is incorporated in the form of a transparency value assigned to each data point (see Fig. 6 for details). The sum of eigenvalues indicates the total scattering power and is assigned to a transparency value using a logarithmic scale (in decibels). This additional feature is essential in order to allow for a meaningful interpretation of the H/α scatter plots at different horizontal layers of the 3-D data set.

3) *Preparation of the Data Cubes for Analysis*: The analyses of the 3-D SAR data cubes that are presented in the Results section are all made with respect to a ground reference in the

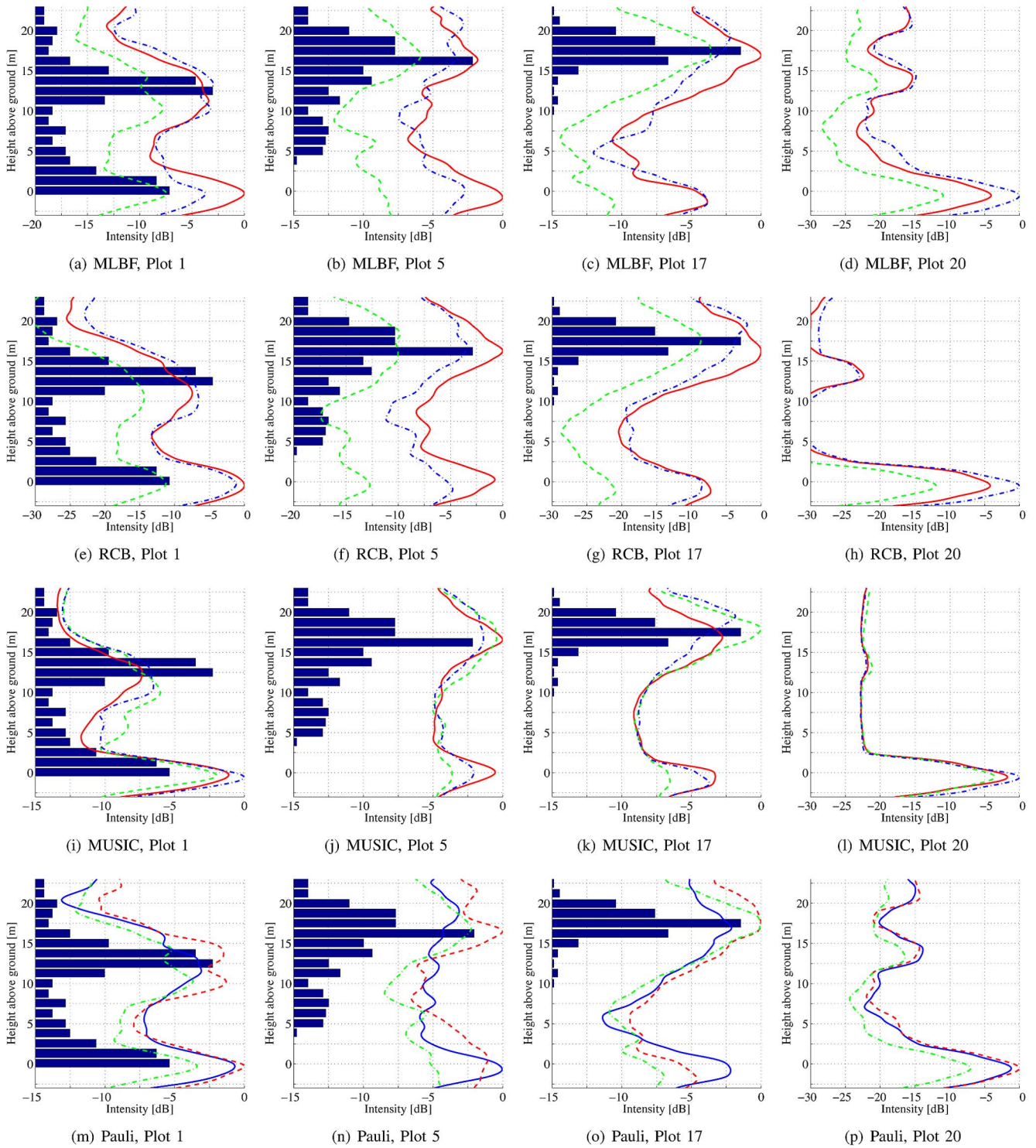


Fig. 3. Vertical profiles of relative intensities from L-band tomographic data of (Plots 1, 5, and 17) a forest and (Plot 20) grassland, respectively, averaged over a circular sample plot of 300 m² for the polarimetric channels (—) HH, (---) HV, and (- · -) VV, MLBF, RCB, and MUSIC, as well as the Pauli basis (—) HH + VV, (---) HH - VV, and (- · -) 2 * HV. For comparison, the histograms of height differences between the ALS DSM and the ALS DEM are underlaid as an external estimate of the distribution of tree heights (see also Fig. 5). (a) MLBF, Plot 1. (b) MLBF, Plot 5. (c) MLBF, Plot 17. (d) MLBF, Plot 20. (e) RCB, Plot 1. (f) RCB, Plot 5. (g) RCB, Plot 17. (h) RCB, Plot 20. (i) MUSIC, Plot 1. (j) MUSIC, Plot 5. (k) MUSIC, Plot 17. (l) MUSIC, Plot 20. (m) Pauli, Plot 1. (n) Pauli, Plot 5. (o) Pauli, Plot 17. (p) Pauli, Plot 20.

form of the DEM from ALS. Prior to any analysis, the data cubes were interpolated in the vertical direction to a sample spacing of 0.15 m, and each vertical column was then shifted vertically by a number of voxels corresponding to the point of

intersection of the ALS DEM and the 3-D voxel grid at each easting/northing position. Thus, all height values given in the comparison of SAR tomography profiles and ALS scanning data are now given relative to the ALS DEM. This means that

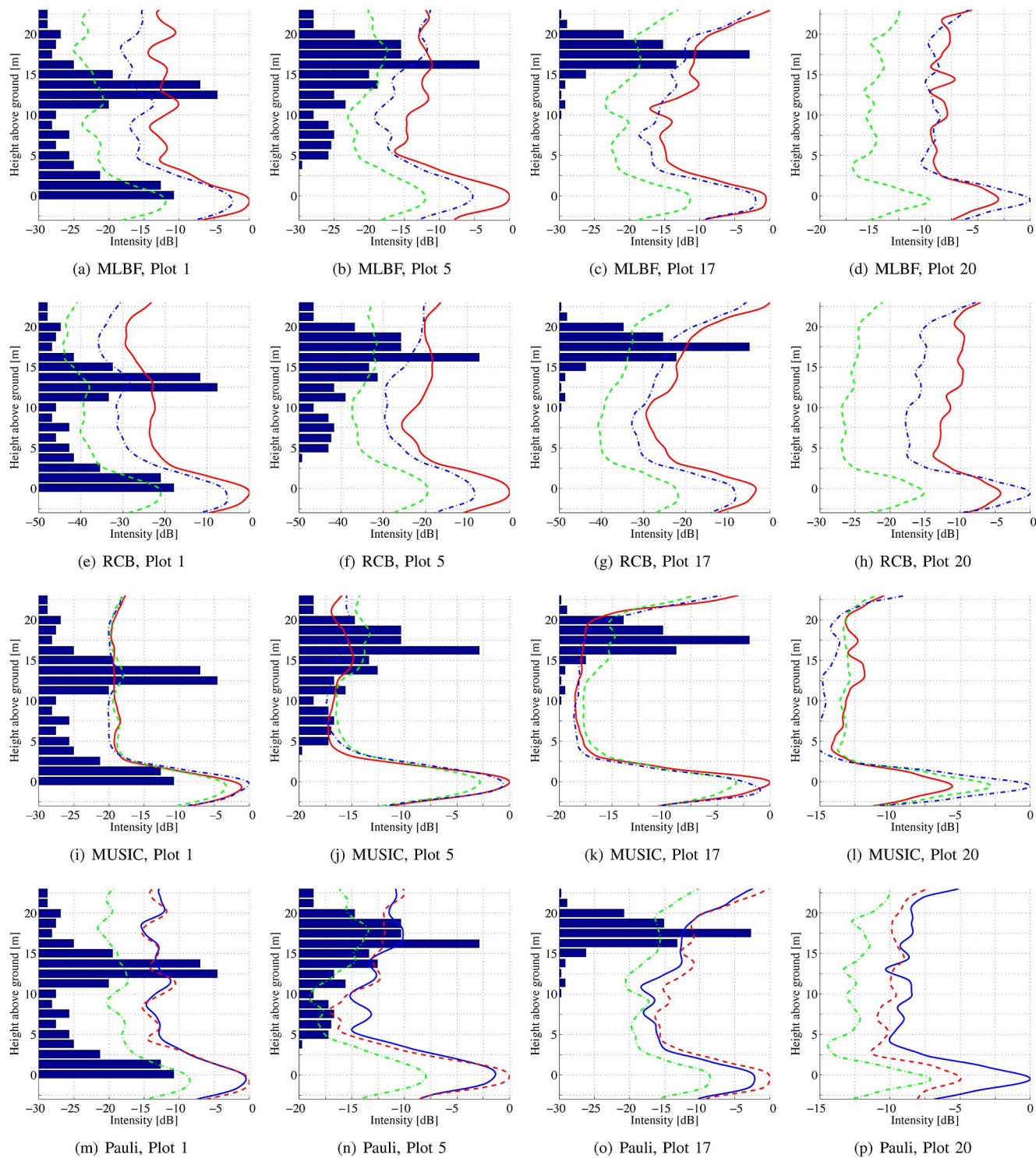


Fig. 4. Vertical profiles of relative intensities from P-band tomographic data of (Plots 1, 5, and 17) a forest and (Plot 20) grassland, respectively, averaged over a circular sample plot of 300 m² for the polarimetric channels (—) HH, (---) HV, and (· · ·) VV, MLBF, RCB, and MUSIC, as well as the Pauli basis (—) HH + VV, (---) HH - VV, and (· · ·) 2 * HV. For comparison, the histograms of height differences between the ALS DSM and the ALS DEM are overlaid as an external estimate of the distribution of tree heights (see also Fig. 5). (a) MLBF, Plot 1. (b) MLBF, Plot 5. (c) MLBF, Plot 17. (d) MLBF, Plot 20. (e) RCB, Plot 1. (f) RCB, Plot 5. (g) RCB, Plot 17. (h) RCB, Plot 20. (i) MUSIC, Plot 1. (j) MUSIC, Plot 5. (k) MUSIC, Plot 17. (l) MUSIC, Plot 20. (m) Pauli, Plot 1. (n) Pauli, Plot 5. (o) Pauli, Plot 17. (p) Pauli, Plot 20.

a *relative height* = 0 m is equivalent to “0 m above ground” or, more accurately, “0 m above the reference DEM from ALS.” Thus, the basis for any analysis given in this paper is a modified

data cube that has a “flat” horizontal ground elevation at every position and that exhibits an interpolated sample spacing of 0.15 m in the vertical direction.

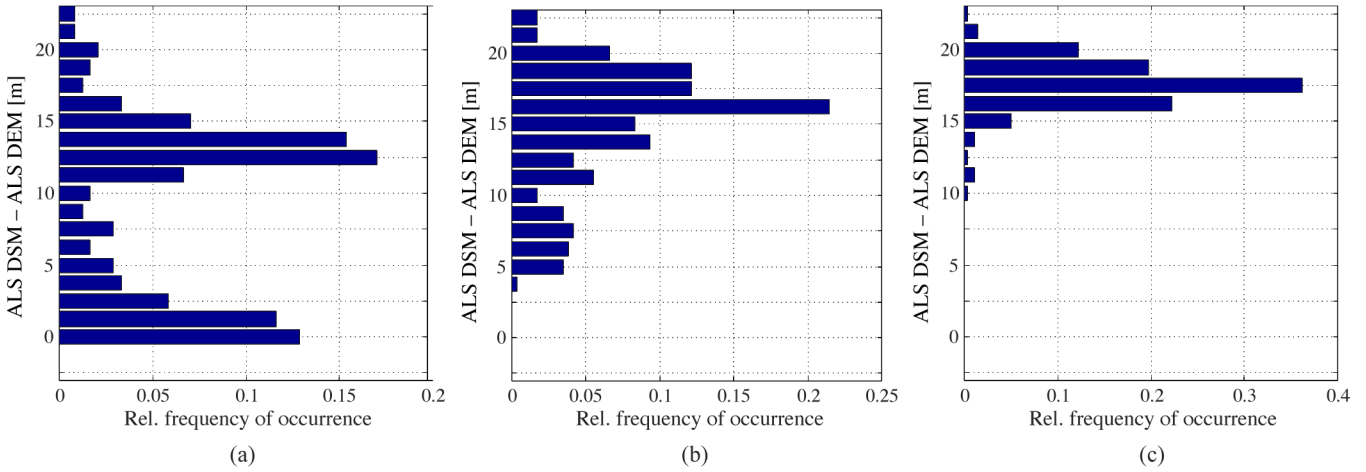


Fig. 5. Distribution of tree heights occurring within the respective sample plots as estimated by the histograms of height differences between the ALS DSM and the ALS DEM. (a) Plot 1. (b) Plot 5. (c) Plot 17.

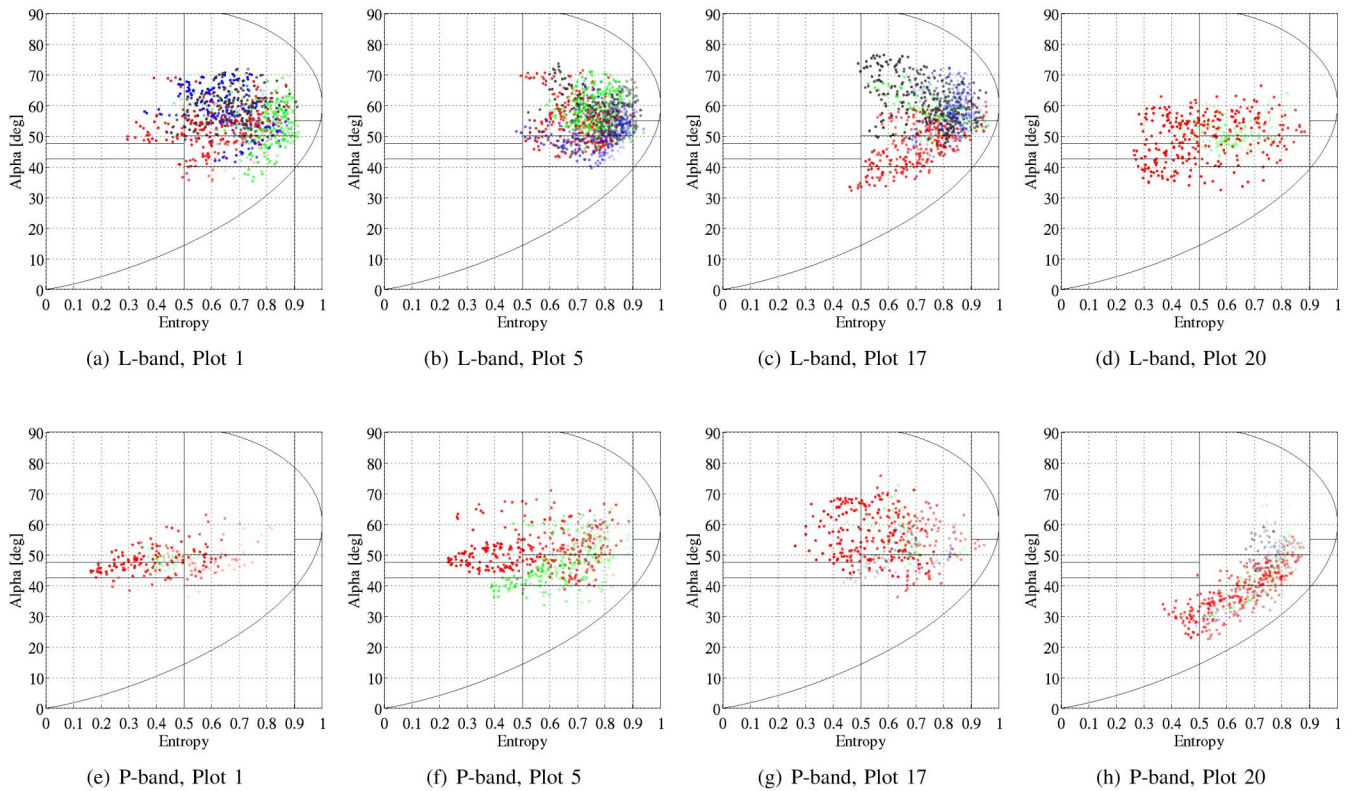


Fig. 6. Entropy/ α scatter plot for different horizontal slices centered at (red) 0, (green) 5, (blue) 10, and (black) 15 m above ground (using the ALS-derived DEM as the reference). The entropy/ α data points of each slice are plotted using transparency scaling based on the sum of the eigenvalues of the $bft3$ coherence matrix: 0dB \rightarrow opaque, ≤ -25 dB \rightarrow transparent. (a) L-band, Plot 1. (b) L-band, Plot 5. (c) L-band, Plot 17. (d) L-band, Plot 20. (e) P-band, Plot 1. (f) P-band, Plot 5. (g) P-band, Plot 17. (h) P-band, Plot 20.

III. EXPERIMENTAL RESULTS

A. Vertical Profiles

In Figs. 3 and 4, for L- and P-bands, respectively, the vertical profiles of relative intensities obtained by averaging the focused profiles of ground-level adjusted tomographic data over a circular sample plot of 300 m² are shown. Profile plots are given for the polarimetric channels HH, HV, and VV for the three beamforming techniques used for focusing in the normal

direction, namely, MLBF, RCB, and MUSIC, as well as for the Pauli basis. The sample plots with numbers 1, 5, and 17 are situated within the forest, whereas the plot number 20 is located on a meadow outside the forested area, with the intention to provide a reference plot that is not subject to volume scattering at canopy level. For the same sample plots, histograms of the difference between the DSM and the DEM obtained from ALS were calculated, which are used as a cross-reference estimate of tree heights occurring within a sample plot. The histograms

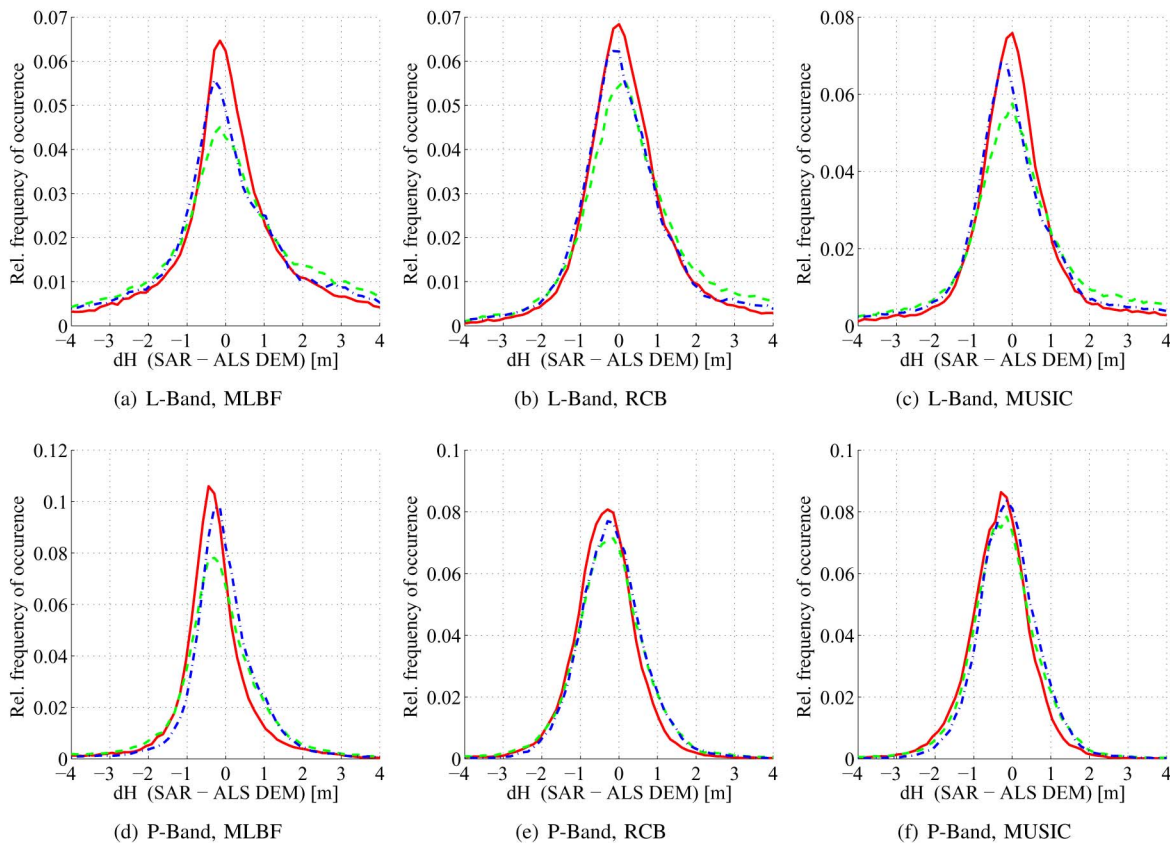


Fig. 7. Ground-level detection below canopy at L- and P-bands: Within a vertical window of ± 4 m around the ground level, as indicated by the ALS DEM, the relative vertical position of the maximum intensity value was determined for all pixels within the forested area. The resulting histograms are depicted for the polarization channels (—) HH, (---) HV, and (- · -) VV, and the three focusing techniques MLBF, RCB, and MUSIC. (a) L-band, MLBF. (b) L-band, RCB. (c) L-band, MUSIC. (d) P-band, MLBF. (e) P-band, RCB. (f) P-band, MUSIC.

are shown in Fig. 5 and are also underlaid to the profile plots in Figs. 3 and 4 in order to ease the comparison.

B. Entropy/ α Scatter Plots

In order to discriminate the dominant scattering mechanisms, the entropy/ A/α decomposition at different height levels within the DEM-adjusted 3-D SAR data cube was calculated for the four sample plots. In Fig. 6, entropy/ α scatter plots are depicted for different horizontal layers at (red) 0, (green) 5, (blue) 10, and (black) 15 m above ground. The entropy/ α data points of each layer are plotted using a transparency scaling which is based on the sum of the eigenvalues of the $\mathbf{T3}$ coherence matrix (0 dB \rightarrow opaque, ≤ -25 dB \rightarrow transparent).

C. Ground-Level Detection

The quality assessment of the ground-level detection is based on the assumption that the maximum intensity value within a vertical window of ± 4 m around the ground level, as indicated by the ALS DEM, represents the location where the backscattering at ground level actually occurs. The relative vertical position of the maximum intensity value was determined for all pixels within a forested subset of dimension 360 m \times 550 m of the area under study. In Fig. 7 and Table II, for L- and P-bands, respectively, the histograms of the relative vertical positions

TABLE II
MEAN VALUES AND STANDARD DEVIATIONS OF GROUND-LEVEL DETECTION BELOW CANOPY CORRESPONDING TO THE HISTOGRAMS IN FIG. 7

L-Band	MLBF		RCB		MUSIC	
	μ	σ	μ	σ	μ	σ
HH	0.18 m	1.77 m	0.29 m	1.37 m	0.16 m	1.47 m
HV	0.27 m	2.07 m	0.49 m	1.68 m	0.32 m	1.87 m
VV	0.15 m	1.96 m	0.27 m	1.53 m	0.14 m	1.70 m
P-Band	MLBF		RCB		MUSIC	
	μ	σ	μ	σ	μ	σ
HH	-0.31 m	1.02 m	-0.37 m	0.90 m	-0.34 m	0.87 m
HV	-0.18 m	1.23 m	-0.25 m	1.06 m	-0.22 m	0.97 m
VV	-0.04 m	1.00 m	-0.19 m	0.93 m	-0.11 m	0.85 m

of the maximum intensity value, as well as the corresponding mean values, and standard deviations are given. They indicate the quality of ground-level detection below canopy, as obtained for the polarization channels HH, HV, and VV and the three focusing techniques MLBF, RCB, and MUSIC.

IV. DISCUSSION

A. Vertical Profiles

At L-band, pronounced local maxima are found at both ground and canopy levels in the vertical profiles of relative

backscattering intensities (see Fig. 3). In Plot 1, for the MLBF data, distinct backscattering at canopy level occurs between 7.5 and 16 m, with maxima around 12 m in the HH channel, 10 m in the HV channel, and between 10 and 13 m in the VV channel. In Plot 5, the maximum at canopy level is found around 16–17 m in the HH and HV channels, whereas no distinct maximum is observed in the VV channel in the case of the MLBF data set—the RCB and MUSIC beamformers, however, yield a pronounced maximum at the same location. Plot 17 shows high average backscattering intensity around 17–18 m in the HH and HV channels and 18–19 m above ground in the VV channel.

All three beamforming methods consistently yield intensity maxima at the same locations while the individual shape of the profiles depends on the beamforming method with the unsurprising tendency that the high- and superresolution methods, i.e., RCB and MUSIC, deliver more pronounced maxima or a reduced clutter level, respectively. MUSIC beamforming destroys the intensity ratio between the polarization channels.

The maxima of the histograms of the forest tree heights from laser scanning data (see Fig. 5) are found around 12.5 m above ground for Plot 1, 16.25 m for Plot 5, and 17.5 m for Plot 17. From the coinciding locations of the maxima in the intensity profiles and the histograms, it can be inferred that the intensity profiles reflect the distribution of tree heights found within a sample plot. This leads to the conclusion that, *at L-band, coherent backscattering within the canopy layer occurs predominantly in the tree-top region* for the forest under study. In Plot 20, which represents grassland outside the forested area, the backscattering at ground level is clearly visible, accompanied by an anomalous sidelobe, which is well suppressed only by the MUSIC beamformer. Yet, visible in the MLBF- and RCB-focused data, the decibel level of the anomalous sidelobe is on a lower level compared to the signal stemming from the microwave interaction at canopy level in Plots 1, 5, and 17.

At P-band, very much in contrast to the L-band case, the ratio between the backscattering intensity at canopy level and that at ground level is very low (see Fig. 4). Without previous knowledge, the canopy level can hardly be localized, at least in the MLBF data set. Nonetheless, a notion of backscattering measured at canopy level can be observed in some channels for the RCB and MUSIC data sets. A consistent detection of the canopy level seems to be unrealistic; the best results would be obtained if only the HV channel was used for the localization of the backscattering within the canopy layer. Throughout all plots, backscattering predominantly, if not exclusively, occurs at ground level. Somewhat surprisingly, this observation is made in all polarization channels. The same behavior was also observed by Tebaldini *et al.* [48], [49] for a different P-band data set. In addition, compared to the L-band case, the unambiguous height appears to be smaller, such that strong ghost target detection occurs around 20 m above ground, particularly in Plot 17. Plot 20 again shows the profile for the grassland. In contrast to the L-band case, the signal-to-clutter ratio is rather small using MLBF, since grassland is not a strong backscattering element at wavelengths of 0.75–1 m. A much better detection of the ground level is obtained by MUSIC beamforming.

B. Entropy/ α Scatter Plots

At L-band, for Plots 1 and 5, backscattering at all height levels is predominantly classified as medium-entropy multiple scattering (Z4), medium-entropy vegetation scattering (Z5), as well as some low-entropy multiple scattering (Z7) for Plot 1 (see Fig. 6). Only for Plot 17, a clear separation in the entropy/ α plane is observed between the contribution at ground level and that at canopy level, respectively. The distribution of tree heights in Fig. 5 reveals that, in Plots 1 and 5, a well-developed understory is present, whereas in Plot 17, no understory is identified. This explains why only in Plot 17 distinct surface scattering is found at ground level. The relatively strong backscattering that is observed within some of the slices centered at 5 m above ground has its origin in the fact that, in order to calculate the T_3 coherency matrix, a spatial averaging is needed. Thus, through the averaging process in combination with the limited Fourier resolution in normal direction (2 m for L-band and 3 m for P-band), signal contributions that actually stem from the ground level are attributed to the slice 5 m above ground.

At P-band, relevant backscattering is virtually exclusively found at ground level. Plot 1 exhibits a somewhat complementary picture to the L-band case: backscattering at ground level is primarily classified as low-entropy dipole (Z8) and low-entropy multiple scattering (Z7). A possible explanation for the high portion of volume scattering detected at ground level within the forest, as found in Plots 5 and 17, is the moderately nonzero slope of the underlying terrain.

Substantial surface scattering is found for the grassland sample plot at P-band (Plot 20), whereas at L-band, a mixed picture of mostly medium-entropy scattering is present.

C. Ground-Level Detection

As is readily observed in Fig. 7 and Table II, the ground level is properly detected at both L- and P-bands. At L-band, the average vertical position of the maximum intensity within a window of ± 4 m around the reference ground level from ALS lies between 0.15 and 0.49 m, indicating a slightly positive bias compared to the reference ground level. The best standard deviation (1.37 m) is achieved for RCB of the HH channel. At P-band, the ground level is underestimated on average by -0.04 to -0.37 m with respect to the cross-reference data. The standard deviations range from 0.85 to 1.23 m with the best value obtained for MUSIC beamforming of the VV channel. In general, the detection of the ground level is slightly better at P-band, as indicated by the narrower shape of the histograms and the lower standard deviations. This outcome is in line with the results obtained from analyzing the profile plots and the entropy/ α plots, where strong backscattering at ground level has also been found at both frequencies with higher relative intensity values at P-band.

V. CONCLUSION

An extensive analysis of polarimetric SAR tomography data sets of a forested area, for the first time at both L- and P-band

frequencies, has been presented. Three data products obtained by time-domain-based MLBF, RCB, and MUSIC beamforming have been investigated for each frequency.

At L-band, the main backscattering contributions are observed at both the ground level and around the tree top. RCB- and MUSIC-beamforming-based vertical profiles exhibit a more distinct tomographic image by increasing the signal-to-clutter ratio and the resolution in normal direction. Thus, in order to just detect the location of the main backscattering contributions, they provide an improved performance compared to MLBF.

A comparison of the vertical profiles of relative intensities of the SAR tomography data and the histograms of the tree heights, as estimated from the difference between the DSM and the DEM from ALS, revealed a striking difference in terms of the location of dominant backscatterers for the two wavelengths: At L-band, coherent backscattering from the canopy (mostly in the tree-top region) is present in all polarization channels, whereas at P-band, only the HV channel exhibits a (still very moderate) local maximum at the canopy level. We conclude that, at P-band, the canopy of the forest under study is virtually transparent to the microwaves, whereas at L-band, both the forest canopy and the ground level are detected. Somewhat unexpectedly, at P-band, the main scattering within the forest occurs at the ground level, not only in the HH and VV channels but *also in the cross-polarized channels*. The same behavior was also observed by Tebaldini *et al.* [48], [49] for a different P-band data set.

Within the forest, surface scattering is very limited even at L-band. Only for Plot 17, where no understory is present, (medium entropy) surface scattering is shown by the entropy/ α scatter plot. Interestingly, the backscattering classification does not change much as a function of height within the forest volume at L-band. This indicates that backscattering sources at ground level and within the canopy layer are not necessarily distinguishable only by their polarimetric signature. At P-band, where scattering at the ground level dominates, the entropy/ α plots show hardly any surface scattering but mostly dipole and volume scattering.

The ground level is well detected at both L- and P-bands and in all polarization channels; the detection of the ground level is slightly superior at P-band though.

As mentioned, the study is limited insofar that only a sector of 30 m in normal direction can be imaged unambiguously, which renders regions of higher canopy out of the scope of this analysis. However, for the selected sample plots, which feature tree heights within this limit, the actual location and type of backscattering mechanisms within the conifer-dominated forest were successfully assessed at L- and P-bands with the help of experimental polarimetric SAR tomography data sets.

In view of the potential upcoming mission BIOMASS, it is interesting to note that, at P-band, coherent backscattering occurs at the ground level. Thus, mapping of the terrain underneath foliage by means of SAR interferometry is a potential scenario. On the other hand, repeat-pass interferometry at P-band is limited due to the small bandwidth assigned at this frequency range, due to the resulting moderate resolution and, to some extent, also due to temporal decorrelation effects.

Looking at the fact that, at L-band, two main locations of backscattering sources could be identified—canopy top and ground level—a single-pass interferometric system, such as sketched in the Tandem-L proposal, appears to be favorable compared to a pure repeat-pass imaging system at L-band.

An open question is to what extent backscattering sources at the various height levels within a forest can be separated reliably in cases where only a very limited number of baselines are available.

ACKNOWLEDGMENT

The authors would like to thank the E-SAR/F-SAR team at the German Aerospace Center (DLR) for their cooperation and technical support and the anonymous reviewers for their valuable comments that improved this paper. They would also like to thank P. Wellig at armasuisse for his wide support and cooperation. This work was conducted at the Remote Sensing Laboratories, University of Zurich, Zurich, Switzerland.

REFERENCES

- [1] M. L. Imhoff, "Radar backscatter and biomass saturation: Ramifications for global biomass inventory," *IEEE Trans. Geosci. Remote Sens.*, vol. 33, no. 2, pp. 511–518, Mar. 1995.
- [2] J. Hagberg, L. Ulander, and J. Askne, "Repeat-pass SAR interferometry over forested terrain," *IEEE Trans. Geosci. Remote Sens.*, vol. 33, no. 2, pp. 331–340, Mar. 1995.
- [3] R. N. Treuhaft, S. N. Madsen, M. Moghaddam, and J. J. van Zyl, "Vegetation characteristics and underlying topography from interferometric radar," *Radio Sci.*, vol. 31, no. 6, pp. 1449–1485, 1996.
- [4] S. R. Cloude and K. P. Papathanassiou, "Polarimetric SAR interferometry," *IEEE Trans. Geosci. Remote Sens.*, vol. 36, no. 5, pp. 1551–1565, Sep. 1998.
- [5] R. N. Treuhaft and S. R. Cloude, "The structure of oriented vegetation from polarimetric interferometry," *IEEE Trans. Geosci. Remote Sens.*, vol. 37, no. 5, pp. 2620–2624, Sep. 1999.
- [6] A. Reigber and A. Moreira, "First demonstration of airborne SAR tomography using multibaseline L-band data," *IEEE Trans. Geosci. Remote Sens.*, vol. 38, no. 5, pp. 2142–2152, Sep. 2000.
- [7] J.-S. Lee, S. R. Cloude, K. P. Papathanassiou, M. R. Grunes, and I. H. Woodhouse, "Speckle filtering and coherence estimation of polarimetric SAR interferometry data for forest applications," *IEEE Trans. Geosci. Remote Sens.*, vol. 41, no. 10, pp. 2254–2263, Oct. 2003.
- [8] R. N. Treuhaft, B. E. Law, and G. P. Asner, "Forest attributes from radar interferometric structure and its fusion with optical remote sensing," *BioScience*, vol. 54, no. 6, pp. 561–571, Jun. 2004.
- [9] B. Hallberg, G. Smith, A. Olofsson, and L. M. H. Ulander, "Performance simulation of spaceborne P-band SAR for global biomass retrieval," in *Proc. IEEE Int. Geosci. Remote Sens. Symp.*, Sep. 2004, pp. 503–506.
- [10] O. Frey, F. Morsdorf, and E. Meier, "Tomographic processing of multibaseline P-band SAR data for imaging of a forested area," in *Proc. IEEE Int. Geosci. Remote Sens. Symp.*, Jul. 2007, pp. 156–159.
- [11] O. Frey, F. Morsdorf, and E. Meier, "Tomographic imaging of a forested area by airborne multi-baseline P-band SAR," *Sensors*, vol. 8, no. 9, pp. 5884–5896, Sep. 2008.
- [12] M. Nannini, R. Scheiber, and A. Moreira, "Estimation of the minimum number of tracks for SAR tomography," *IEEE Trans. Geosci. Remote Sens.*, vol. 47, no. 2, pp. 531–543, Feb. 2009.
- [13] R. N. Treuhaft, B. D. Chapman, J. R. dos Santos, F. G. Gonçalves, L. V. Dutra, P. M. L. A. Graça, and J. B. Drake, "Vegetation profiles in tropical forests from multibaseline interferometric synthetic aperture radar, field, and lidar measurements," *J. Geophys. Res.*, vol. 114, no. D23 110, pp. 1–16, Dec. 2009.
- [14] F. Garestier, P. C. Dubois-Fernandez, D. Guyon, and T. Le Toan, "Forest biophysical parameter estimation using L- and P-band polarimetric SAR data," *IEEE Trans. Geosci. Remote Sens.*, vol. 47, no. 10, pp. 3379–3388, Oct. 2009.
- [15] S. Tebaldini, "Algebraic synthesis of forest scenarios from multibaseline PolInSAR data," *IEEE Trans. Geosci. Remote Sens.*, vol. 47, no. 12, pp. 4132–4142, Dec. 2009.

- [16] Candidate earth explorer core mission BIOMASS—Report for assessment, ESA, Frascati, Italy, Tech. Rep. ESA SP-1313/2. [Online]. Available: http://esamultimedia.esa.int/docs/SP1313-2_BIOMASS.pdf
- [17] F. Hélière, C. Lin, F. Fois, M. Davidson, A. Thompson, and P. Bensi, "BIOMASS: A P-band SAR Earth explorer core mission candidate," in *Proc. IEEE Radar Conf.*, May 2009, pp. 1–6.
- [18] A. Moreira, G. Krieger, I. Hajnsek, K. Papathanassiou, M. Eineder, F. D. Zan, M. Younis, and M. Werner, "Tandem-L: Monitoring the Earth's dynamics with InSAR and Pol-InSAR," in *Proc. PolInSAR*, Frascati, Italy, Jan. 2009, (ESA SP-668).
- [19] G. Krieger, I. Hajnsek, K. P. Papathanassiou, M. Eineder, M. Younis, F. De Zan, P. Prats, S. Huber, M. Werner, H. Fiedler, A. Freeman, P. Rosen, S. Hensley, W. Johnson, L. Villeux, B. Grafmueller, R. Werninghaus, R. Bamler, and A. Moreira, "The Tandem-L mission proposal: Monitoring Earth's dynamics with high resolution SAR interferometry," in *Proc. IEEE Radar Conf.*, May 2009, pp. 1–6.
- [20] A. Donnellan, P. Rosen, J. Graf, A. Loverro, A. Freeman, R. Treuhart, R. Oberto, M. Simard, E. Rignot, R. Kwok, X. Pi, J. Blair, W. Abdalati, J. Ranson, H. Zebker, B. Hager, H. Shugart, M. Fahnestock, and R. Dubayah, "Deformation, ecosystem structure, and dynamics of ice (DESDynI)," in *Proc. IEEE Aerospace Conf.*, Mar. 2008, pp. 1–13.
- [21] M. C. Dobson, F. T. Ulaby, T. LeToan, A. Beaudoin, E. S. Kasischke, and N. Christensen, "Dependence of radar backscatter on coniferous forest biomass," *IEEE Trans. Geosci. Remote Sens.*, vol. 30, no. 2, pp. 412–415, Mar. 1992.
- [22] H. Israelsson, L. M. H. Ulander, J. L. H. Askne, J. E. S. Fransson, P.-O. Frörlind, A. Gustavsson, and H. Hellsten, "Retrieval of forest stem volume using VHF SAR," *IEEE Trans. Geosci. Remote Sens.*, vol. 35, no. 1, pp. 36–40, Jan. 1997.
- [23] R. F. Nelson, P. Hyde, P. Johnson, B. Emessiene, M. L. Imhoff, R. Campbell, and W. Edwards, "Investigating RaDAR-LiDAR synergy in a North Carolina pine forest," *Remote Sens. Environ.*, vol. 110, no. 1, pp. 98–108, Sep. 2007.
- [24] P. Pasquali, C. Prati, F. Rocca, M. Seymour, J. Fortuny, E. Ohlmer, and A. J. Sieber, "A 3-D SAR experiment with EMSL data," in *Proc. IEEE Int. Geosci. Remote Sens. Symp.*, 1995, vol. 1, pp. 784–786.
- [25] C. Jakowatz and P. Thompson, "A new look at spotlight mode synthetic aperture radar as tomography: Imaging 3-D targets," *IEEE Trans. Image Process.*, vol. 4, no. 5, pp. 699–703, May 1995.
- [26] J. Homer, I. Longstaff, and G. Callaghan, "High resolution 3-D SAR via multi-baseline interferometry," in *Proc. IEEE Int. Geosci. Remote Sens. Symp.*, May 1996, vol. 1, pp. 796–798.
- [27] J. Li, Z.-S. Liu, and P. Stoica, "3-D target feature extraction via interferometric SAR," *Proc. Inst. Elect. Eng.—Radar, Sonar Navig.*, vol. 144, no. 2, pp. 71–80, Apr. 1997.
- [28] L. Rössing and J. H. Ender, "Multi-antenna SAR tomography using superresolution techniques," in *Proc. EUSAR—Special Issue, Frequenz, Zeitschrift für Telekommunikation (J. Telecommun.)*, Mar. 2001, vol. 55, pp. 123–128.
- [29] P. Berardino, G. Fornaro, R. Lanari, E. Sansosti, F. Serafino, and F. Soldovieri, "Multi-pass synthetic aperture radar for 3-D focusing," in *Proc. IEEE Int. Geosci. Remote Sens. Symp.*, 2002, vol. 1, pp. 176–178.
- [30] F. Bordononi, F. Lombardini, F. Gini, and A. Jakobsson, "Multibaseline cross-track SAR interferometry using interpolated arrays," *IEEE Trans. Aerosp. Electron. Syst.*, vol. 41, no. 4, pp. 1473–1482, Oct. 2005.
- [31] G. Fornaro, F. Serafino, and F. Soldovieri, "Three-dimensional focusing with multipass SAR data," *IEEE Trans. Geosci. Remote Sens.*, vol. 41, no. 3, pp. 507–517, Mar. 2003.
- [32] F. Gini, F. Lombardini, and M. Montanari, "Layover solution in multibaseline SAR interferometry," *IEEE Trans. Aerosp. Electron. Syst.*, vol. 38, no. 4, pp. 1344–1356, Oct. 2002.
- [33] F. Lombardini, M. Montanari, and F. Gini, "Reflectivity estimation for multibaseline interferometric radar imaging of layover extended sources," *IEEE Trans. Signal Process.*, vol. 51, no. 6, pp. 1508–1519, Jun. 2003.
- [34] Z. Su, Y. Peng, and X. Wang, "Feature-independent aperture evaluator for the curvilinear SAR," *IEEE Geosci. Remote Sens. Lett.*, vol. 4, no. 2, pp. 191–195, Apr. 2007.
- [35] F. Lombardini and M. Pardini, "3-D SAR tomography: The multibaseline sector interpolation approach," *IEEE Geosci. Remote Sens. Lett.*, vol. 5, no. 4, pp. 630–634, Oct. 2008.
- [36] M. Pardini, F. Lombardini, and F. Gini, "The hybrid Cramér–Rao bound on broadside DOA estimation of extended sources in presence of array errors," *IEEE Trans. Signal Process.*, vol. 56, no. 4, pp. 1726–1730, Apr. 2008.
- [37] G. Fornaro and A. Pauciuolo, "LMMSE 3-D SAR focusing," *IEEE Trans. Geosci. Remote Sens.*, vol. 47, no. 1, pp. 214–223, Jan. 2009.
- [38] F. Lombardini and A. Reigber, "Adaptive spectral estimation for multi-baseline SAR tomography with airborne L-band data," in *Proc. IEEE Int. Geosci. Remote Sens. Symp.*, 2003, vol. 3, pp. 2014–2016.
- [39] S. Guillaso and A. Reigber, "Polarimetric SAR Tomography (POLTOM-SAR)," in *Proc. PolInSAR*, Frascati, Italy, 2005.
- [40] O. Frey and E. Meier, "Combining time-domain back-projection and Capon beamforming for tomographic SAR processing," in *Proc. IEEE Int. Geosci. Remote Sens. Symp.*, 2008, pp. II-445–II-448.
- [41] ESA, PolInSAR 2009 Sorted Recommendations, Frascati, Italy, 2009, Jan. [Online]. Available: http://earth.esa.int/workshops/polinsar2009/POLInSAR2009_sorted_rec.pdf
- [42] O. Frey, C. Magnard, M. Rüegg, and E. Meier, "Focusing of airborne synthetic aperture radar data from highly nonlinear flight tracks," *IEEE Trans. Geosci. Remote Sens.*, vol. 47, no. 6, pp. 1844–1858, Jun. 2009.
- [43] O. Frey and E. Meier, "3-D time-domain SAR imaging of a forest using airborne multibaseline data at L- and P-bands," *IEEE Trans. Geosci. Remote Sens.*, vol. 49, no. 10, pp. 3660–3664, Oct. 2011.
- [44] S. R. Cloude and E. Pottier, "A review of target decomposition theorems in radar polarimetry," *IEEE Trans. Geosci. Remote Sens.*, vol. 34, no. 2, pp. 498–518, Mar. 1996.
- [45] S. R. Cloude and E. Pottier, "An entropy based classification scheme for land applications of polarimetric SAR," *IEEE Trans. Geosci. Remote Sens.*, vol. 35, no. 1, pp. 68–78, Jan. 1997.
- [46] S. R. Cloude, J. Fortuny, J. M. Lopez-Sanchez, and A. J. Sieber, "Wideband polarimetric radar inversion studies for vegetation layers," *IEEE Trans. Geosci. Remote Sens.*, vol. 37, no. 5, pp. 2430–2441, Sep. 1999.
- [47] J.-S. Lee, M. R. Grunes, T. L. Ainsworth, L.-J. Du, D. L. Schuler, and S. R. Cloude, "Unsupervised classification using polarimetric decomposition and the complex Wishart classifier," *IEEE Trans. Geosci. Remote Sens.*, vol. 37, no. 5, pp. 2249–2258, Sep. 1999.
- [48] S. Tebaldini, F. Rocca, and A. Monti-Guarnieri, "Model based SAR tomography of forested areas," in *Proc. IEEE Int. Geosci. Remote Sens. Symp.*, Jul. 2008, vol. 2, pp. II-593–II-596.
- [49] S. Tebaldini and F. Rocca, "Polarimetric options for SAR tomography of forested areas," in *Proc. PolInSAR*, Frascati, Italy, Jan. 2009, ESA SP-668.



Othmar Frey (S'04–M'08) received the M.Sc. degree in geomatic engineering from Swiss Federal Institute of Technology (ETH) Zurich, Zurich, Switzerland, in 2002 and the Ph.D. (Dr. sc. nat.) degree (with distinction) in remote sensing from the University of Zurich, Zurich, in 2010.

From 2002 to 2010, he was a Research Associate with the Remote Sensing Laboratories, University of Zurich, where he worked on a geometric error budget analysis for TerraSAR-X data products and on atmospheric effects in synthetic aperture radar

(SAR) data until 2003/2004. Since then, he has mainly been working in the field of SAR signal processing with emphasis on airborne SAR imaging and SAR tomography. He has developed and implemented SAR signal-processing software that allows for end-to-end data processing of advanced imaging modes, such as airborne multibaseline SAR and SAR data acquisitions from nonlinear flight tracks. Since 2011, he has been with the Chair of Earth Observation and Remote Sensing, Institute of Environmental Engineering, ETH Zurich, as a Senior Research Scientist, and with GAMMA Remote Sensing AG, Gmüliigen, Switzerland.

Dr. Frey has contributed to invited sessions on SAR tomography at the 2008 European Conference on Synthetic Aperture Radar (EUSAR) and the IEEE International Geoscience and Remote Sensing Symposia in 2008, 2009, and 2010. He was the recipient of the 3rd Place Student Paper Award at the 2010 EUSAR Conference in Aachen, Germany, and the ETH medal for an outstanding M.Sc. thesis. He was the corecipient of the Best Paper Award at the ISPRS Workshop Laserscanning and Silvilaser 2007 in Helsinki, Finland.



Erich Meier (A'09) received the M.Sc. degree in geography and the Ph.D. (Hons.) degree in remote sensing from the University of Zurich, Zurich, Switzerland, in 1982 and 1989, respectively.

From 1979 to 1982, he was a Research Assistant with the Remote Sensing Section and, from 1982 to 1983, with the GIS Laboratory, Department of Geography, University of Zurich. From 1983 to 2006, he was a Research Scientist with the Remote Sensing Laboratories (RSL), Department of Geography, University of Zurich, where he is currently the Research Section Head involved in teaching as well as in research in digital image processing, software development for computer graphics, and radiometric and geometric calibrations of SAR and optical imagery. Since 2000, he has been the Head of the SARlab, a research group within RSL. The main research interests of this group are the development of new focusing algorithms for SAR data from UHF to millimeter wave, interferometry, polarimetry, and moving target indication algorithms, as well as calibration and validation activities for spaceborne and airborne systems. He is responsible for the research strategies as well as the organization of the team. He is a Consultant on behalf of several national and international organizations and private companies.